PCCP

PAPER

View Article Online
View Journal | View Issue

NO oxidation catalysis on copper doped hexagonal phase $LaCoO_3$: a combined experimental and theoretical study†

Cite this: *Phys. Chem. Chem. Phys.*, 2014, **16**, 5106

Chen Zhou,‡[a] Xiao Liu,‡[bc] Chunzheng Wu,[a] Yanwei Wen,[c] Yejian Xue,[a] Rong Chen,[b] Zhaoliang Zhang,[d] Bin Shan,*[c] Hongfeng Yin*[a] and Wei Guo Wang[a]

Received 24th November 2013,
Accepted 18th January 2014

DOI: 10.1039/c3cp54963a

www.rsc.org/pccp

Cobalt-based perovskite catalysts showed excellent performance towards NO–NO_2 oxidation. We systematically investigated the influence of different levels of Cu-doping on the catalytic performance of hexagonal phase $LaCoO_3$ ($LaCo_{1-x}Cu_xO_3$ (x = 0.1, 0.2, 0.3)) for NO oxidation. The catalytic activities of the oxide catalysts followed the sequence: $LaCo_{0.9}Cu_{0.1}O_3$ > $LaCoO_3$ > $LaCo_{0.8}Cu_{0.2}O_3$ > $LaCo_{0.7}Cu_{0.3}O_3$ where the highest NO conversion for $LaCo_{0.9}Cu_{0.1}O_3$ was 82% at 310 °C. The relevant structural characterizations were conducted by XRD, BET, FTIR and TEM. The interaction between Co and Cu promoted the conversion of NO to NO_2. Upon increasing the Cu doping content, a decrease of the performance resulted from the generation of isolated CuO on the surface of the oxides, confirmed using H_2-TPR and XPS. Combined with first-principle calculations, we explored the reaction mechanism of NO oxidation on the surface and found that Cu doping would facilitate the reaction by decreasing the energy of oxygen vacancy formation and the NO_2 desorption barrier from Co- or Cu-nitrite.

1. Introduction

Diesel and lean-burn gasoline engines have aroused great interest for their higher fuel efficiency, low cost and high stability. However, the resulting pollutants NO_x should be removed due to the harm caused by them to human-beings and the environment. In order to meet the increasingly stringent NO_x regulations, two promising technologies for reducing the emission of NO_x, NO_x selective catalytic reduction (SCR) and lean-burn NO_x trap (LNT) have been developed. For both technologies, NO_2 is a critical intermediate species because it enhances the activity and facilitates the transformation of pollutants.[1,2] For the SCR reaction utilizing NH_3, the reaction rate can be improved dramatically in the presence of NO_2 equaling the NO concentration and leading to a so called fast SCR reaction: $2NH_3 + NO + NO_2 \rightarrow 2N_2 + 3H_2$.[3–6] For another case, NO_2 can be readily absorbed on the surface of LNT catalysts.[7,8] NO_2 is also considered to be an acceptable choice for soot removal as it has shown good activity to oxidize soot at low temperatures.[9–11] Thus, NO–NO_2 oxidation is a vital step in the treatment of the diesel exhaust. Traditionally, Pt-based catalysts are mainly utilized to catalyze NO oxidation in the lean-burn stage and NO_x reduction in the rich-burn stage because of their excellent catalytic performance. However, high cost, poor thermal durability and agglomeration restrict their practical application in next generation emission technologies.[12,13] Therefore, it is desirable to develop substitute materials for the precious metals to reduce material cost and improve the performance of the exhaust treatment catalyst.

In the past years, perovskite oxides with larger cations at A-site and smaller cations at B-site have attracted much attention due to their high activity in CO oxidation, volatile organic compounds (VOC) oxidation, NO_x storage and reduction.[12,14–20] Recently, they have also been shown to catalyze NO oxidation very efficiently. Shen's group evaluated the effects of the B-site substitute $LaMO_3$ (M = Mn, Fe, Co) towards the NO oxidation reaction, and Co-based perovskite oxides were among the most promising candidates as NO oxidation catalysts.[21] They also found that doping of Co into $LaMnO_3$ ($LaMn_{0.9}Co_{0.1}O_3$) could also improve the catalytic performance for NO oxidation.[22] Wen *et al.* reported Ce doping in $LaCoO_3$ and the results showed that

[a] *Division of Fuel Cell & Energy Technology, Ningbo Institute of Material Technology and Engineering, Chinese Academy of Sciences, Ningbo 315201, Zhejiang, People's Republic of China. E-mail: yinhf@nimte.ac.cn*
[b] *State Key Laboratory of Digital Manufacturing Equipment and Technology and School of Mechanical Science and Engineering, Huazhong University of Science and Technology, Wuhan 430074, Hubei, People's Republic of China*
[c] *State Key Laboratory of Material Processing and Die and Mould Technology and School of Materials Science and Engineering, Huazhong University of Science and Technology, Wuhan 430074, Hubei, People's Republic of China. E-mail: bshan@hust.edu.cn*
[d] *College of Chemistry and Chemical Engineering, University of Jinan, Jinan 250022, Shandong, People's Republic of China*

† Electronic supplementary information (ESI) available. See DOI: 10.1039/c3cp54963a

‡ Chen Zhou and Xiao Liu contributed equally to this work.

20% Ce-doping could enhance $LaCoO_3$'s catalytic efficiency on NO conversion.[23] Furthermore, Li's group reported that the introduction of Sr into $LaCoO_3$ at the A-site improved the NO conversion significantly,[12] and found Sr-doped $LaCoO_3$ rival the performance of commercial Pt-based catalysts.

Generally, it is found that the perovskite compounds with lanthanum in the A-site and/or cobalt in the B-site have shown excellent performance for NO oxidation and the partial substitution of the cation A by A′ and/or B by B′ can alter the perovskite stability, redox performance or catalytic activity. Kaliaguine *et al.* reported that the introduction of Cu into the B-site of $LaCoO_3$ led to an increase in the production of alcohols and the high uniform dispersion of the metallic Cu–Co played a key role in the synthesis of higher alcohols.[24,25] Cu-substituted perovskite $LaCoO_3$ also promoted the performance of the partial oxidation of methane and anti-coking according to the report of Toniolo's group.[26] However, its application in NO oxidation in the context of emission control has not been systematically studied to the best of our knowledge. We have developed a series of Cu-doped hexagonal phase $LaCoO_3$ catalysts for NO oxidation. In this report, we evaluated the catalytic activity of different Cu-doped $LaCoO_3$ samples and found the activities of the oxides to follow the sequence: $LaCo_{0.9}Cu_{0.1}O_3$ > $LaCoO_3$ > $LaCo_{0.8}Cu_{0.2}O_3$ > $LaCo_{0.7}Cu_{0.3}O_3$. The maximum NO conversion was 82% at 310 °C for $LaCo_{0.9}Cu_{0.1}O_3$, which exhibited better performance than Pt-based catalysts at high temperature (T > 270 °C) and the pure phase perovskite catalyst $LaCoO_3$. The relationships between physicochemical properties and catalytic performance of Cu-doped $LaCoO_3$ for NO oxidation were also discussed. The reaction pathways of NO oxidation on the surface of pure and Cu-doped $LaCoO_3$ were investigated by the first-principles plane wave method. The results showed that Cu doping would lower the desorption barrier of NO_2 from the surface nitrite species and facilitate the NO oxidation. Our work showed that Cu-doped $LaCoO_3$ could be a candidate material for a low cost and high activity NO oxidation catalyst, and shed light on the mechanism of the improved performance due to Cu-doping.

2. Experimental section

2.1 Synthesis of perovskite-type oxides

The Cu doped $LaCoO_3$ perovskite oxides were synthesized using a modified sol–gel method with citric acid (CA) and ethylenediamine tetraacetic acid (EDTA) as complexing agents.[27]

In this paper, perovskite-type oxides with the formula $LaCo_{1-x}Cu_xO_3$ (x = 0, 0.1, 0.2, 0.3) are hereafter designated as LCC10 × x. For example, $LaCo_{0.9}Cu_{0.1}O_3$ is abbreviated as LCC1.

2.2 Characterizations

The phase structure analysis of the perovskite powders was carried out by X-ray diffraction (XRD) at room temperature. XRD analyses were performed on a Bruker D8 Advance operating at 40 kV and 40 mA with a Cu Kα1 radiation source (λ = 0.154056 nm) at a stepwise increase of 0.02° s^{-1} in the Bragg angle (2θ) range from 10° to 90°.

The specific surface area (SSA) of all samples was measured by nitrogen absorption at 77 K using a Micromeritics ASAP 2020M physisorption analyzer. The samples were degassed at 300 °C overnight prior to analysis.

The Fourier transform IR (FTIR) spectra of the samples were obtained in the absorbance mode in a Bruker Tensor 27 spectrophotometer. Spectra were obtained at 4 cm^{-1} resolution averaging 32 scans.

Transmission electron microscopy (TEM) and high-resolution transmission electron microscopy (HRTEM) images were obtained using a JEM 2100 microscope operated at 200 kV.

X-ray Photoelectron Spectroscopy (XPS) studies were characterized on an AXIS ULTRADLD Multifunctional X-ray Photoelectron Spectroscope with an Al Kα radiation source at room temperature and under a vacuum pressure of 10^{-7} Pa (10^{-9} Torr). The starting angle of the photoelectron was set at 90°.

The temperature programmed experiments were carried out on a FINESORB3010 instrument (Zhejiang Finetec Co.) with a thermal conductivity detector (TCD). For the H_2 temperature programmed reduction (H_2-TPR) test, 30 mg of the oxides was loaded into the U-type quartz tube reactor. TPR profiles were recorded using a 10% H_2–Ar mixture (50 mL min^{-1}). Prior to reduction, the sample was pretreated at 300 °C for 1 hour using a stream of 21% O_2/N_2 (70 mL min^{-1}) and then cooled down to room temperature. The temperature was retained at room temperature for 30 minutes and then increased o 800 °C at a rate of 5 °C min^{-1}, and kept at 800 °C for 30 minutes. The consumption of H_2 was determined using a TCD with Ar gas as the reference gas.

2.3 Activity test

Catalytic activity was measured by NO oxidation under lean conditions by using the same reactor with H_2-TPR with a 3 mm internal diameter of the reactor tube. For each test, 50 mg of the catalyst was used, with the temperature measured using a K-type thermocouple in direct contact with the upper quartz wool near the powder. The total feed flow rate was 150 mL min^{-1}, corresponding to a space velocity of 180 000 mL (g^{-1} h^{-1}). The effluent gas was analyzed using an ECO Physics CLD822Mh chemiluminescent NOx analyzer. The feed composition of the mixture gas was 400 ppm NO, 10% O_2 and N_2 as the balance gas. The furnace was ramped at 2 °C min^{-1} from room temperature to 400 °C. The conversion of NO is defined as the percentage of NO feed that has reacted:

$$X(\%) = \frac{NO_{in} - NO_{out}}{NO_{in}} \times 100$$

NO_{in} is the NO concentration in the inlet gas and NO_{out} is the NO concentration in the outlet gas.

2.4 Computational methods

Density functional theory (DFT)[28,29] calculations were carried out using plane waves as implemented in Vienna *ab initio* simulation package (VASP).[30–32] The exchange and correlation energy was treated by generalized gradient approximation (GGA) with the Perdew–Burke–Ernzerhof (PBE)[33] form generated using the projector augmented wave (PAW)[34] method. The geometry

optimization was considered complete when the Hellmann–Feynman force on each atom was less than 0.05 eV $Å^{-1}$ and an energy cutoff of 400 eV was employed on the plane wave basis. The k points were sampled on a Monkhorst–Pack[35] grid of size 7 × 7 × 3 for bulk structural calculations, which was well converged within 5 meV in total energy, compared to the one of size 9 × 9 × 5.

In order to discuss the thermodynamic stability of the surfaces, we calculated the surface grand potential, which had been applied to binary and ternary compounds,[36,37] for the low-index crystal planes. A vacuum thickness of 15 Å was adopted to avoid the interaction between periodic slabs. Moreover, the atomic layers and surface area of the slabs were enough for accurate results. The surface grand potential per unit area, Ω, introduced at the chemical potential μ_O and μ_{Co} of O and Co atomic species was defined as:

$$\Omega = \frac{1}{2S}[E_{slab} - N_{La}E_{bulk} - \mu_O(N_O - 3N_{La}) - \mu_{Co}(N_{Co} - N_{La})] \quad (1)$$

where E_{slab} and E_{bulk} were the energy of the slab and primitive cell bulk, N_{La}, N_{Co} and N_O were the number of atoms in the slab and the factor of 1/2 corresponded to the same termination of the top and bottom slabs. Boundary conditions have been considered to define the accessible region of a thermo-dynamical system.[37] It was easy to find four confinements as follows:

$$\mu_{La} \le \mu^0_{La} \quad (2)$$

$$\mu_{Co} \le \mu^0_{Co} \quad (3)$$

$$\mu_O \le \mu^0_O \quad (4)$$

$$\mu_{La} + \mu_{Co} + 3\mu_O \ge E_{LaCoO_3} \quad (5)$$

where μ^0_{La} and μ^0_{Co} were the total energies of the perfect La and Co crystals per formula unit La and Co, respectively, and μ^0_O was $E_{O_2}/2$, where E_{O_2} was the energy of an O_2 molecule. E_{LaCoO_3} was the total energy of bulk per formula unit $LaCoO_3$.

A climbing nudged elastic band (NEB)[38] calculation was used to calculate the minimum energy path (MEP) and found the saddle points between two local minima for the system. Initial approximations to reaction paths were obtained by linear interpolation between the energy minima configurations. Eight intermediate images were used for all NEB calculations, which was sufficient to map the MEP accurately.

3. Results and discussions

3.1 Structure characterizations

XRD patterns shown in Fig. 1 indicated that all samples exhibited the typical hexagonal perovskite structure in JCPDS 25-1060. However, the main peaks of Cu doped $LaCoO_3$ shifted to a lower 2θ angle, implying the expansion of the $LaCoO_3$ lattice. This was in agreement with the calculated lattice parameters in Table 1, which increased with increasing Cu doping content. This suggested that Cu entered into the lattice of the $LaCoO_3$ perovskite structure and the introduction of the larger

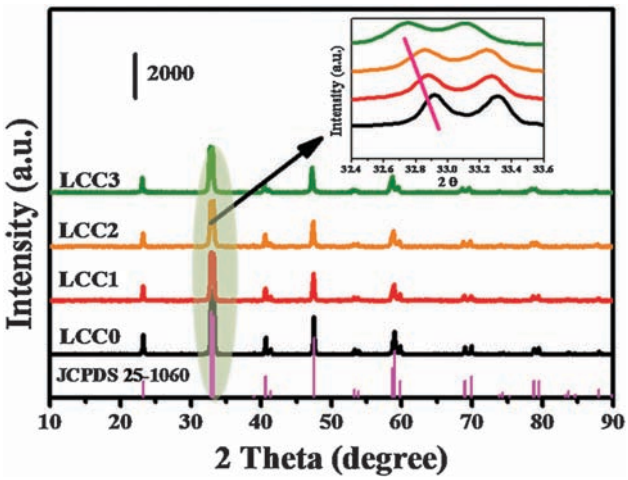

Fig. 1 XRD patterns of the LCC oxides.

Table 1 Lattice parameters and BET specific surface areas of the oxides

Sample	Lattice parameters			BET surface area ($m^2\ g^{-1}$)
	a (Å)	b (Å)	c (Å)	
LCC0	5.441	5.441	13.11	3.91
LCC1	5.451	5.451	13.12	4.02
LCC2	5.461	5.461	13.15	6.33
LCC3	5.468	5.468	13.17	5.93

sized Cu^{2+} (0.73 Å) into the B-site than Co^{3+} (0.61 Å) enlarged the lattice.[24,26,39,40]

The BET specific area of the prepared samples is also shown in Table 1. The BET surface area for pure LCC0 was 3.91 $m^2\ g^{-1}$, with those of Cu doped samples lying between 4.02 and 6.33 $m^2\ g^{-1}$.

The crystalline asymmetry of the perovskite materials could also be determined by the IR vibration frequencies in the infrared region of the lattice oxygen (800–400 cm^{-1}). Fig. 2 presents the FTIR spectra of the obtained oxide catalysts. The band at 598 cm^{-1} with the shoulder peak at 558 cm^{-1} (ν_1 mode) and the band at 420 cm^{-1} (ν_2 mode) were observed for $LaCoO_3$. The bands corresponded to the Co–O bond in the perovksite lattice with a rhombohedral structure.[41,42] With the introduction of Cu into the B-site, the ν_2 mode disappeared and ν_1 mode with a shoulder became weaker, especially for LCC3 with the maximum Cu content. This indicated that the symmetry of the perovskite was improved by Cu doping. Similar results were observed by Y. Wu *et al.*[43,44]

Fig. 3 showed TEM and HRTEM images of LCC0 and LCC1. From TEM images, the particle size of the synthesized perovskite oxide catalysts was found to be in the range of 80 nm to 100 nm. Meanwhile, the lattice spacing of 0.28 nm consistent with the $(11\bar{2}0)$ plane (Fig. 3c and d) for LCC0 and LCC1 was clearly observed.

3.2 TPR

The reducibility of the oxides with Cu doping was investigated using H_2-TPR measurements and was compared with the reduction of CuO as shown in Fig. 4. For LCC0, two clear reduction regions were observed at the low temperature region

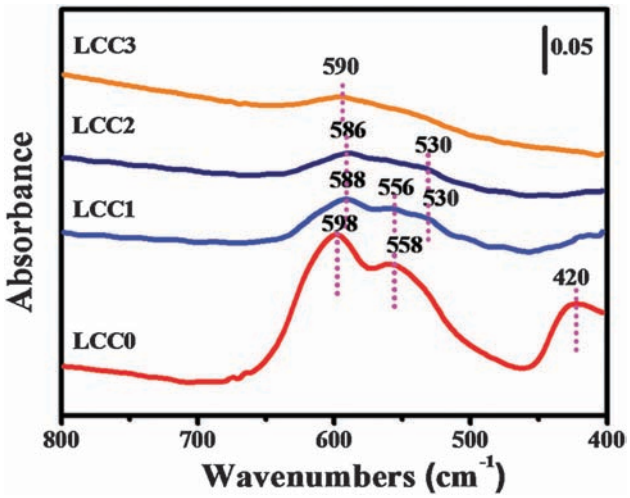

Fig. 2 FT-IR spectra of LCC oxides.

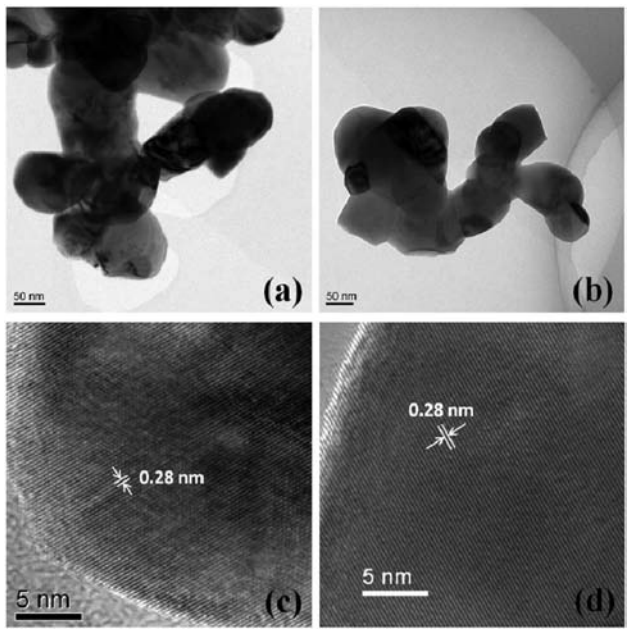

Fig. 3 (a) TEM image and (c) HRTEM image of LCC0 and (b) TEM image and (d) HRTEM image of LCC1.

(peaks 1 and 2) and the high temperature region (peak 3). At a low-temperature range of 200–450 °C, peaks 1 and 2 were attributed to the reduction of Co^{3+} to Co^{2+}, yet the high-temperature peak 3 (450–600 °C) was ascribed to the reduction of Co^{2+} to Co^0.[25,45] For the Cu doped samples, the reduction peaks were observed at lower temperatures compared with that of LCC0, suggesting that Cu could promote the reducibility of neighboring Co ions[24,26] and the interaction did exist between Cu and Co. For LCC1, with small amount of Cu doping, four reduction peaks were observed. Peak 1 was attributed to the reduction of the absorbed oxygen, which was lower than the reduction temperature of CuO. Peak 2 was close to the reduction temperature of CuO, implying that some isolated CuO remained.

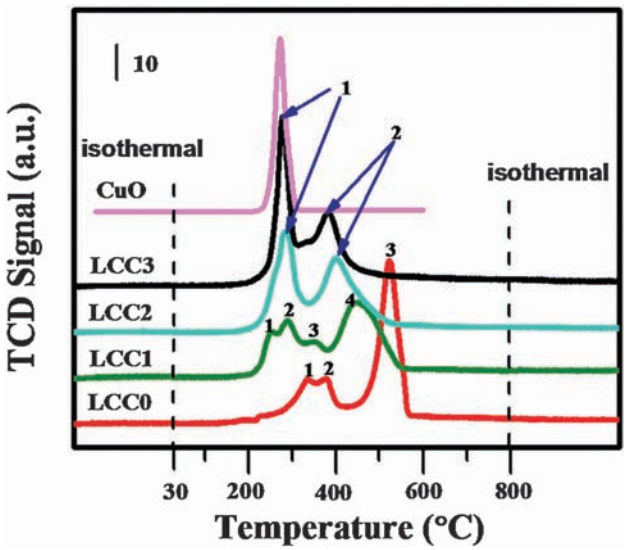

Fig. 4 H_2-TPR profile of the LCC oxide catalysts. The display values of TCD signal of CuO are equal to the measured values * 0.15.

This indicated the enrichment of CuO on the surface of the oxides. Peaks 3 and 4 were ascribed to the reduction of Co^{3+} to Co^{2+} and Co^{2+} to Co^0, respectively. These reductions occurred at lower temperatures than that of LCC0. Upon further increasing the Cu doping content, the obtained TPR became different in the cases of LCC2 and LCC3 against LCC1. The reductions at higher temperatures continued to be lowered for both samples. However, the reduction of surface oxygen at lower temperature became weaker (LCC2) and even disappeared (LCC3). Conversely, the reduction of isolated CuO at 277 °C (peak 1) was prevailing for LCC2 and LCC3. This suggested that the surfaces of LCC2 and LCC3 were predominated by isolated CuO.

3.3 XPS

XPS is a powerful tool to investigate the surface compositions and the chemical valence state. Table 2 displays the surface information based on the XPS results for the LCC oxides. From Table 2, the amount of Cu on the surface increased while the amount of Co decreased sharply with increasing Cu content. In order to understand the influence of Cu introduction, we focused on the XPS spectra of Cu $2p_{3/2}$ presented in Fig. 5. An asymmetric Cu $2p_{3/2}$ spectrum at BE = 934.1 eV with the broad satellite peak of the Cu $2p_{3/2}$ band (characteristic of Cu^{2+} ions) was observed, and the binding energy of Cu $2p_{3/2}$ in CuO was reported at 933.2 ± 0.2 eV.[46] The higher binding energy of Cu ions in the Cu-doped samples compared with that of CuO might be attributed to the

Table 2 Surface components (mass ratio) of the samples from XPS data (nominal values in parentheses)

Sample	La	Co	Cu	O	Cu/Co
LCC0	22.73	11.51 (23.97)	—	65.14	—
LCC1	21.43	7.96 (21.53)	4.66 (2.58)	65.95	0.58 (0.11)
LCC2	20.62	7.06 (19.10)	5.62 (5.15)	66.71	0.79 (0.25)
LCC3	20.12	6.22 (16.69)	7.19 (7.71)	66.46	1.15 (0.43)

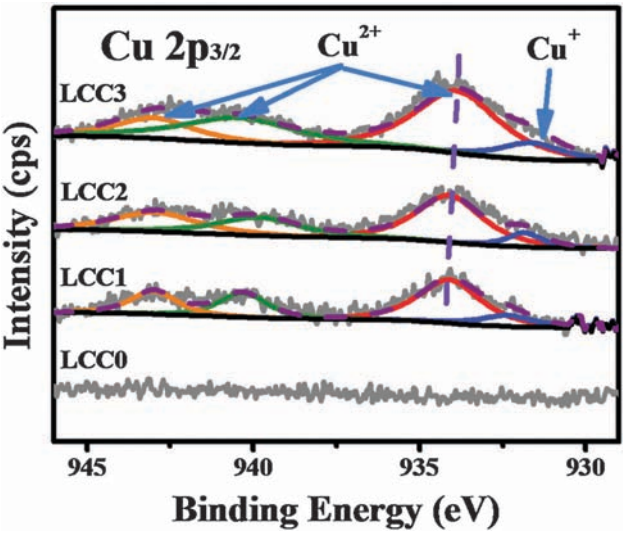

Fig. 5 XPS spectra of Cu $2p_{3/2}$ as a function of composition.

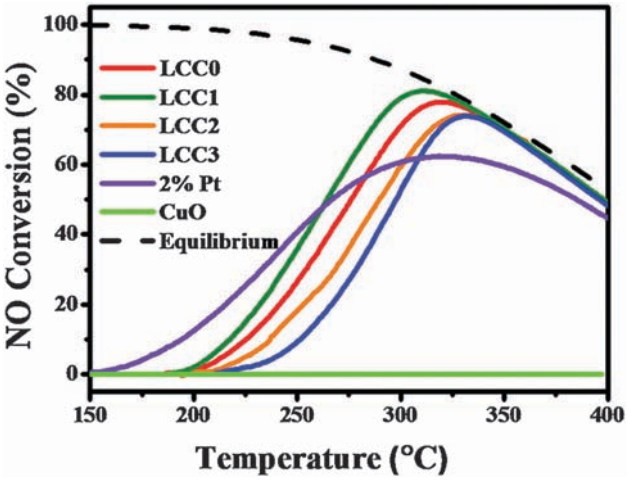

Fig. 6 The conversion of NO oxidation as a function of temperature and composition: 400 ppm NO, 10% O_2 and a balance of N_2.

effect of the ionic coordinate structure of LCC oxides around Cu^{2+} ions in agreement with the report by Tabata *et al.* for Cu doping $LaMnO_3$ samples.[47] Upon increasing the Cu content, the binding energy of Cu $2p_{3/2}$ decreased from 934.5 eV (LCC1) to 933.8 eV (LCC3), close to the corresponding binding energy of CuO. This also demonstrated the formation of isolated CuO on the surface detected by H_2-TPR, which was in accordance with the fact that the calculated surface Cu/Co atomic ratios increased with the increase in Cu content as listed in Table 2. Additionally, another XPS peak of Cu $2p_{3/2}$ assigned to Cu^+ species was also distinguished at 932 eV.[46] The presence of Cu^+ could be attributed to the interaction between Cu and Co, which rendered Cu^{2+} with easier reducibility as shown in H_2-TPR results (Fig. 4). With the increase in Cu content, the binding energy of Co $2p_{3/2}$ (shown in Fig. S1, ESI†) decreased since the valence of Cu is lower than that of Co; therefore, the introduction of Cu into the B-site led to the generation of higher oxidation of B-site ions (Co^{3+} to Co^{4+}) and/or the formation of oxygen vacancies in order to preserve the charge neutrality.

3.4 Activity evaluation

The catalytic activity of the as-synthesized perovskite oxide catalysts towards NO oxidation is shown in Fig. 6. For all LCC oxide catalysts, no NO conversions were observed when the temperature of the catalyst bed was lower than 200 °C and NO conversion began to increase at 200 °C, achieving its maximum around 310–320 °C for different samples before dropping down due to thermodynamic limitations. Among these catalysts, $LaCoO_3$ showed a maximum conversion of 78% at 320 °C, similar to Li's work of 77% at 325 °C.[12] The introduction of a small amount of Cu into the B-site further improved the performance for NO oxidation. Although LCC1 had a lower specific area than that of LCC2 and LCC3, LCC1 obtained the best NO oxidation performance, the conversion reached 82% at 310 °C. This might be attributed to the interaction between Co and Cu confirmed by the combination of XRD and H_2-TPR and the influence of Cu on the neighboring ions might be the key factor for promoting the catalytic activity of NO to NO_2. Nevertheless, the activities decreased when Cu was further increased to 0.2 and 0.3, and their NO conversions were even inferior to that of LCC0. Introduction of extra Cu into the B-site resulted in the generation of isolated CuO on the surface of the catalysts confirmed by H_2-TPR and XPS, reduced the number of lattice Cu in the perovskite structure on the surface, and thus led to the decrease of the performance. Meanwhile, the catalytic activity of CuO (purchased from Sinopharm Chemical Reagent Co, Ltd) towards NO oxidation was tested as well and no NO conversion was observed as a function of temperature. As a reference sample, 2% Pt/Al_2O_3 was also tested. As shown in Fig. 6, the maximum NO conversion of the commercial Pt-based catalyst was only 63% at 315 °C. Pt-based catalysts showed better performance than that of LCC1 below 270 °C; however, LCC1 had better activity performance than Pt-based catalysts when the temperature was higher than 270 °C. It is worth noting that the maximum NO conversions of all perovskite samples were higher than that of Pt-based catalysts.

3.5 Reaction mechanism

To gain further understanding into the effects of Cu doping and the NO oxidation on the perovskite surface, DFT calculations and the NEB method were employed. The optimized lattice constants of hexagonal phase $LaCoO_3$ (in Fig. S2(a), ESI†) were $a = b = 5.426$ Å, $c = 12.950$ Å, $\alpha = \beta = 90°$, $\gamma = 120°$, and the other structural parameters are listed in Table S1 (ESI†), which are in good agreement with ours and previous experimental and computational results.[48,49]

In order to discuss the thermodynamic stability of the surfaces, considering the symmetry of the crystal, we calculated the surface grand potential for eight low-index crystal planes, which were $(10\bar{1}0)$-O and $(10\bar{1}0)$-LaCoO terminations, (0001)-LaO and (0001)-Co terminations, $(11\bar{2}0)$-O and $(11\bar{2}0)$-LaCoO terminations, and $(1\bar{1}02)$-CoO and $(1\bar{1}02)$-LaO terminations. The detailed calculation results are listed in Table S2 (ESI†), such as the energy of bulk $LaCoO_3$ (La, Co) and all slabs. The stability of the low-index crystal plane in hexagonal phase $LaCoO_3$ is depicted in Fig. 7, which predicted that only four cases in the eight possible

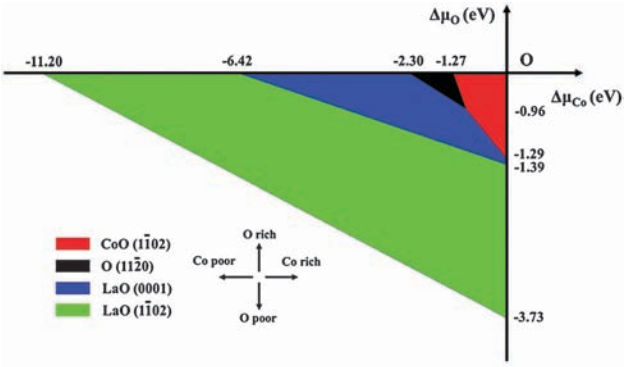

Fig. 7 The stability graph of the hexagonal phase $LaCoO_3$'s low-index crystal plane. The actual most stable termination is represented as a function of the excess O and Co chemical potentials $\Delta\mu_O$ ($\Delta\mu_O = \mu_O - \mu_O^0$, vertical) and $\Delta\mu_{Co}$ ($\Delta\mu_{Co} = \mu_{Co} - \mu_{Co}^0$, horizontal).

terminations would be energetically favorable. The (1$\bar{1}$02)-CoO termination was the most stable in O- and Co-rich environments, while the complementary (1$\bar{1}$02)-LaO was most stable in O- and Co-poor conditions. The (11$\bar{2}$0)-O termination showed a stability domain in a moderate O and Co environment. In particular, under an experimentally relevant oxygen chemical potential of around −0.3 eV to −0.4 eV, the most stable surface changed successively from LaO surface to O surface, and then to CoO termination with increasing Co chemical potential.

As indicated in Fig. S2(b) (ESI†), the O vacancy formation energy of (11$\bar{2}$0)-O termination was 0.68 eV, which would be in the most favorable energy window of around 0.5 to 1.0 eV for NO oxidation. We thus consider the Cu doping effect on this active surface towards NO oxidation. The presence of (11$\bar{2}$0) surfaces were also confirmed in HRTEM images (Fig. 3c). The NO oxidation reaction pathways on an ideal (11$\bar{2}$0)-O terminated $LaCoO_3$ surface are shown in Fig. 8(a). On the O terminated (11$\bar{2}$0) plane, the oxidation reaction initiated with NO(g) adsorbing on the O site to form Co-nitrite ($-NO_2$). Then the adsorbed NO snatched the lattice O to form NO_2(g) and the NO_2(g) desorbed from the surface leaving a lattice O vacancy. This step was considered as the rate-determining step (RDS) with the highest energy barrier of 1.23 eV. The subsequent steps which included oxygen adsorption and NO oxidation by O_2* could proceed with a relatively low barrier. Analyzing the transition states (TS) in blue frameworks, we found the energy barriers were contributed by the Co–O (O–O) bond's broken and NO_2's desorption from the surface with the distance between the Co (O) atom and the O (O) atom being larger as shown in Fig. 8(a). For comparison, we also calculated the NO oxidation pathways upon Cu-doped (11$\bar{2}$0)-O termination as shown in Fig. 8(b). The O vacancy formation energy bonding with Cu atom was calculated to be −0.13 eV, which indicates a spontaneous formation of O vacancies near Cu sites upon (11$\bar{2}$0)-O termination. Therefore, the NO oxidation reaction on the (11$\bar{2}$0)-O termination initiates with an O vacancy on the Cu site. The calculated results indicated the first step was triplet O_2(g) adsorption onto the O vacancy with an energy barrier of 0.46 eV, and reaction with an adsorbed NO molecule with an energy barrier of 0.58 eV.

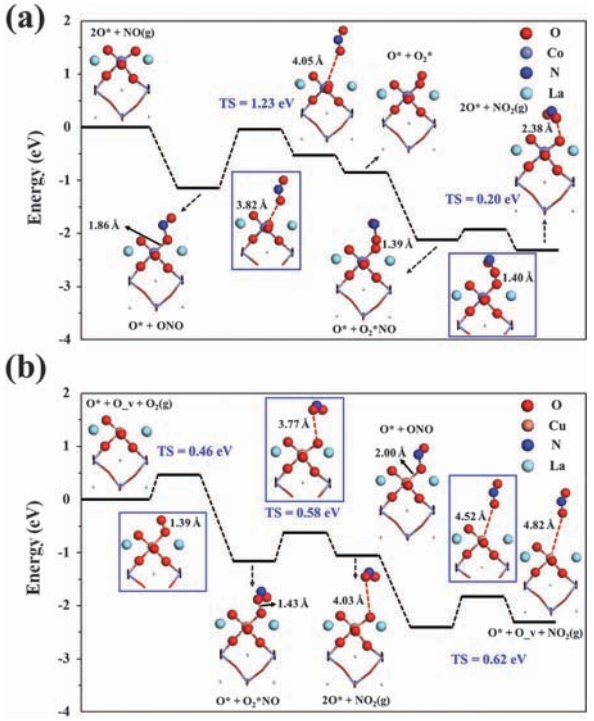

Fig. 8 Stick-ball model of NO oxidation on the (11$\bar{2}$0)-O termination of (a) pure and (b) Cu doped $LaCoO_3$. The structures in the blue frameworks are transition states. The total reaction can be regarded as $2NO + O_2 \rightarrow 2NO_2$ exothermally.

Another NO(g) would subsequently be adsorbed onto the lattice oxygen to form Cu-nitrite ($-NO_2$) species on the surface, with a desorption barrier of 0.62 eV. The NO_2 desorption from the Cu-nitrite constitutes the RDS of the reaction, after which the surface recovers to the initial state. We can see that Cu doping could decrease the barriers of NO_2 desorption substantially and contribute to the enhancement of NO catalytic performance.

4. Conclusions

Cu doped $LaCoO_3$ perovskite oxides synthesized using the modified sol–gel methods were used to catalyze the NO oxidation reaction. LCC1 exhibited the best performance and achieved a NO conversion of 82% at 310 °C. H_2-TPR and XPS indicated that the interaction between Co and Cu existed in the perovskite oxides. However, some isolated CuO was generated on the surface of the samples and the amount of CuO increased upon increasing the doping content and the decrease of the activity was attributed to inactive CuO on the surface. First-principles calculations of reaction pathways showed that the RDS of the NO oxidation reaction was the NO_2 desorption from Co or Cu-nitrite. The introduction of Cu into $LaCoO_3$ makes the reaction energy barrier of such an RDS decrease from 1.23 eV to 0.62 eV. The work investigated the mechanism of Cu-doped perovskite compounds for NO oxidation, providing a viable direction in the search for substitute materials for precious metal catalysts.

Acknowledgements

This work is supported by the National Basic Research Program of China (2013CB934800 and 2011CB606401), National Natural Science Foundation of China (Grant 11004068 and 51101064), Fundamental Research Funds for the Central Universities, HUST (2012TS012 and 2012TS076) and China Postdoctoral Science Foundation (2012M521421). The authors acknowledge Thousand Young Talents Plan and New Century Excellent Talents in University (NCET), and the Texas Advanced Computing Center (TACC) at The University of Texas at Austin (http://www.tacc.utexas.edu) for providing grid resources that have contributed to the research results reported within this paper.

Notes and references

1 M. Tas, R. van Hardeveld and E. M. van Veldhuizen, *Plasma Chem. Plasma Process.*, 1997, **17**, 371–391.
2 I. Atribak, A. Bueno-Lopez, A. Garcia-Garcia and B. Azambre, *Phys. Chem. Chem. Phys.*, 2010, **12**, 13770–13779.
3 L. Olsson, H. Persson, E. Fridell, M. Skoglundh and B. Andersson, *J. Phys. Chem. B*, 2001, **105**, 6895–6906.
4 W. Hauptmann, M. Votsmeier, J. Gieshoff, A. Drochner and H. Vogel, *Appl. Catal., B*, 2009, **93**, 22–29.
5 L. Olsson and E. Fridell, *J. Catal.*, 2002, **210**, 340–353.
6 K. Zhuang, J. Qiu, F. Tang, B. Xu and Y. Fan, *Phys. Chem. Chem. Phys.*, 2011, **13**, 4463–4469.
7 P. J. Schmitz and R. J. Baird, *J. Phys. Chem. B*, 2002, **106**, 4172–4180.
8 P. Forzatti, L. Lietti, I. Nova and E. Tronconi, *Catal. Today*, 2010, **151**, 202–211.
9 Y. Wei, J. Liu, Z. Zhao, A. Duan, G. Jiang, C. Xu, J. Gao, H. He and X. Wang, *Energy Environ. Sci.*, 2011, **4**, 2959–2970.
10 Y. Wei, J. Liu, Z. Zhao, A. Duan and G. Jiang, *J. Catal.*, 2012, **287**, 13–29.
11 J. Oi-Uchisawa, S. Wang, T. Nanba, A. Ohi and A. Obuchi, *Appl. Catal., B*, 2003, **44**, 207–215.
12 C. H. Kim, G. Qi, K. Dahlberg and W. Li, *Science*, 2010, **327**, 1624–1627.
13 D. M. Fernandes, C. F. Scofield, A. A. Neto, M. J. B. Cardoso and F. M. Z. Zotin, *Chem. Eng. J.*, 2010, **160**, 85–92.
14 V. Szabo, M. Bassir, A. Van Neste and S. Kaliaguine, *Appl. Catal., B*, 2002, **37**, 175–180.
15 C. Constantinou, W. Li, G. Qi and W. S. Epling, *Appl. Catal., B*, 2013, **134–135**, 66–74.
16 B. Viswanathan, *Catal. Rev.*, 1992, **34**, 337–354.
17 R. J. Voorhoeve, D. W. Johnson, J. P. Remeika and P. K. Gallagher, *Science*, 1977, **195**, 827–833.
18 R. J. H. Voorhoeve, J. P. Remeika, P. E. Freeland and B. T. Matthias, *Science*, 1972, **177**, 353–354.
19 N. A. Merino, B. P. Barbero, P. Grange and L. E. Cadús, *J. Catal.*, 2005, **231**, 232–244.
20 J. Chen, M. Shen, X. Wang, G. Qi, J. Wang and W. Li, *Appl. Catal., B*, 2013, **134–135**, 251–257.
21 J. Chen, M. Shen, X. Wang, J. Wang, Y. Su and Z. Zhao, *Catal. Commun.*, 2013, **37**, 105–108.
22 J. Wang, Y. Su, X. Wang, J. Chen, Z. Zhao and M. Shen, *Catal. Commun.*, 2012, **25**, 106–109.
23 Y. Wen, C. Zhang, H. He, Y. Yu and Y. Teraoka, *Catal. Today*, 2007, **126**, 400–405.
24 N. Tien-Thao, H. Alamdari, M. H. Zahedi-Niaki and S. Kaliaguine, *Appl. Catal., A*, 2006, **311**, 204–212.
25 N. Tien-Thao, H. Alamdari and S. Kaliaguine, *J. Solid State Chem.*, 2008, **181**, 2006–2019.
26 F. S. Toniolo, R. N. S. H. Magalhães, C. A. C. Perez and M. Schmal, *Appl. Catal., B*, 2012, **117–118**, 156–166.
27 J. Shao, Y. Tao, J. Wang, C. Xu and W. G. Wang, *J. Alloys Compd.*, 2009, **484**, 263–267.
28 P. Hohenberg and W. Kohn, *Phys. Rev.*, 1964, **136**, B864–B871.
29 W. Kohn and L. J. Sham, *Phys. Rev.*, 1965, **140**, A1133–A1138.
30 G. Kresse and J. Hafner, *Phys. Rev. B: Condens. Matter Mater. Phys.*, 1993, **47**, 558–561.
31 G. Kresse and J. Hafner, *Phys. Rev. B: Condens. Matter Mater. Phys.*, 1994, **49**, 14251–14269.
32 G. Kresse and J. Hafner, *Comput. Mater. Sci.*, 1996, **6**, 15–50.
33 J. P. Perdew, K. Burke and M. Ernzerhof, *Phys. Rev. Lett.*, 1996, **77**, 3865–3868.
34 G. Kresse and D. Joubert, *Phys. Rev. B: Condens. Matter Mater. Phys.*, 1999, **59**, 1758–1775.
35 H. J. Monkhorst and J. D. Pack, *Phys. Rev. B: Solid State*, 1976, **13**, 5188–5192.
36 G. H. Chen, Z. F. Hou and X. G. Gong, *Comput. Mater. Sci.*, 2008, **44**, 46–52.
37 F. Bottin, F. Finocchi and C. Noguera, *Phys. Rev. B: Condens. Matter Mater. Phys.*, 2003, **68**, 035418.
38 G. Henkelman and H. Jónsson, *J. Chem. Phys.*, 2000, **113**, 9978–9985.
39 R. D. Shannon, *Acta Crystallogr., Sect. A: Cryst. Phys., Diffr., Theor. Gen. Cryst.*, 1976, **32**, 751–767.
40 P. Porta, S. De Rossi, M. Faticanti, G. Minelli, I. Pettiti, L. Lisi and M. Turco, *J. Solid State Chem.*, 1999, **146**, 291–304.
41 G. Pecchi, C. Campos and O. Peña, *Mater. Res. Bull.*, 2009, **44**, 846–853.
42 E. J. Baran, *Catal. Today*, 1990, **8**, 133–151.
43 Z. Zhao, X. Yang and Y. Wu, *Sci. China, Ser. B: Chem.*, 1997, **40**, 464–474.
44 C. Liu, Z. Zhao, X. Ye and Y. Wu, *Sci. China, Ser. B: Chem.*, 1997, **40**, 512–516.
45 J. A. Villoria, M. C. Alvarez-Galvan, S. M. Al-Zahrani, P. Palmisano, S. Specchia, V. Specchia, J. L. G. Fierro and R. M. Navarro, *Appl. Catal., B*, 2011, **105**, 276–288.
46 J. Ghijsen, L. H. Tjeng, J. van Elp, H. Eskes, J. Westerink, G. A. Sawatzky and M. T. Czyzyk, *Phys. Rev. B: Condens. Matter Mater. Phys.*, 1988, **38**, 11322–11330.
47 K. Tabata, Y. Hirano and E. Suzuki, *Appl. Catal., A*, 1998, **170**, 245–254.
48 P. G. Radaelli and S. W. Cheong, *Phys. Rev. B: Condens. Matter Mater. Phys.*, 2002, **66**, 094408.
49 I. A. Nekrasov, S. V. Streltsov, M. A. Korotin and V. I. Anisimov, *Phys. Rev. B: Condens. Matter Mater. Phys.*, 2003, **68**, 235113.

